

Research papers

Kraft and organosolv lignin-activated carbon composites for supercapacitor electrode materials

Nagore Izaguirre^a, Mikel Alberro^b, Xabier Erdocia^c, Jalel Labidi^{a,*}^a Biorefinery Processes Research Group, Chemical and Environmental Engineering Department, Engineering Faculty of Gipuzkoa, University of the Basque Country UPV/EHU, Plaza Europa 1, 20018 Donostia, Spain^b Biorefinery Processes Research Group, Department of Electronic Technology, Faculty of Engineering, University of the Basque Country (UPV/EHU), Plaza Europa 1, 20018 San Sebastian, Spain^c Biorefinery Processes Research Group, Department of Applied Mathematics, University of the Basque Country UPV/EHU, Rafael Moreno "Pichichi" 3, 48013 Bilbao, Spain

ARTICLE INFO

Keywords:

Kraft lignin
Organosolv lignin
Activated carbon
Ultrasound deposition
Energy storage materials

ABSTRACT

Lignin-activated carbon (AC) composites were employed as electrode active materials to develop more environmentally friendly Supercapacitor (SC) materials with enhanced properties. This way, the hydroquinone/quinone moieties present in lignin molecules added Faradaic processes to the system, and the capacitance of the active material increased, making it appropriate for future applications requiring more efficient and sustainable active materials. Lignin, a sustainable biobased aromatic polymer high in carbon content, was deposited on AC surface employing ultrasound (US) system, and for a better deposition, AC was treated with HNO₃. Since the composition and properties of lignin can vary depending on their isolation process, two different types of lignin were used: Kraft lignin (KL) and Organosolv lignin (OL), and the effects on the chemical and electrochemical composition were deduced. Physicochemical, morphological, and electrochemical analyses were carried out on the lignin-AC composite to determine the optimum material combination and treatment process. It was observed that the acid treatment was effective in enhancing the functionality and porosity of the surface. Additionally, it improved the deposition of lignin and facilitated the formation of hierarchically porous structures on the surface of treated activated carbon (TAC), with different tendencies depending on the lignin employed. The creation of highly porous structures also resulted in enhanced electrochemical performance in materials. This validated the process, where eco-innovative technologies like US forces and employment of lignocellulosic biomass compounds like lignin were used as sustainable and efficient alternatives for obtaining electrochemically active materials.

1. Introduction

Lignin-based electrode materials are gaining interest due to their sustainability and high availability. Most of the works of lignin incorporation into batteries are based on its conversion into carbon materials, and substitution of the currently used non-renewable fossil-based carbons [1]. Lignin is a promising candidate due to its high carbon content and unique aromatic nature. Moreover, by modulating its structure, different carbon materials can be obtained to meet the diverse requirements of different battery types. Porous carbons derived from lignin have been fabricated as active materials of electrodes [2]. Lignin-derived carbons have also been used as active materials in SCs [3], with studies exploring different activation processes, including carbonization and combinations with polymers like polyacrylonitrile (PAN) or

different metal oxides [4]. However, these processes are energy demanding. Therefore, alternative approaches to incorporate lignin into Energy Storage (ES) materials without the need for prior carbonization are gaining interest [1,5–7].

Numerous research works have focused on producing and studying composite or hybrid materials by combining lignin with other carbonaceous materials or conducting polymers. These efforts aim to enhance the properties of the resulting materials. Depending on their targeted application, different properties are needed. Nevertheless, one common characteristic of enhanced properties of carbon materials is their specific surface area (SSA). The porosity is a key factor for the battery performance, as it eases the diffusion kinetics and strengthens the conductivity network of the conductive ions [8]. Activated carbon is a commonly used material for this reason, but different methodologies have been

* Corresponding author.

E-mail address: jalel.labidi@ehu.es (J. Labidi).<https://doi.org/10.1016/j.est.2023.110386>

Received 25 July 2023; Received in revised form 24 October 2023; Accepted 29 December 2023

Available online 9 January 2024

2352-152X/© 2024 The Authors. Published by Elsevier Ltd. This is an open access article under the CC BY-NC-ND license (<http://creativecommons.org/licenses/by-nc-nd/4.0/>).

carried out to increase the SSA and pore size distribution (PSD), for a further enhanced specific capacitance [9–11]. AC is used for many different applications, ranging from adsorbents to ES devices, all needing high SSA for better performance. It is also relatively inexpensive, stable, and easily processable. Several methods have been carried out to increase the SSA of AC. The most widely used method is the treatment with concentrated HNO_3 [12–14]. Other works have studied the effect of different concentrations of HNO_3 solutions for the AC treatment, which have verified that the concentrated HNO_3 brings the best results [15]. This treatment not only increases the porosity of the surface of the material but also increases the oxygen-containing functional groups, subsequently enhancing its performance [16–18]. Although the SSA plays an important role in the improvement of the capacity, it does not necessarily mean that all the pores will be electrochemically accessible in contact with the electrolyte. Indeed, the type of pore plays an important role, since mesopores (2–50 nm wide pores) can adsorb more and larger ions than micropores (<2 nm wide pores) [19]. Nevertheless, micropore-sized carbon SCs have been proven to contribute to charge storage by absorbing electrolyte ions bigger than the pores of the carbon [20].

Another approach for enhanced carbon SCs is the fabrication of hybrid materials or composites. Double-layer (DL) carbon materials have been combined with pseudocapacitance materials to expand their capacitance. This enhancement occurs due to the addition of Faradaic processes happening on the redox groups of the pseudocapacitance materials [21]. A sustainable approach to the synthesis of hybrid materials is the incorporation of lignin into AC materials. Lignin is the second most abundant polymer on earth and is considered a plausible substitute for many materials, such as ES device materials [22]. It is regarded to be a pseudocapacitance material due to the hydroquinone/quinone moieties present in its molecules. Combining these lignin properties with the non-Faradaic processes happening in AC, more sustainable materials with enhanced capacitance can be obtained. Therefore, another current target in the development of novel ES device materials is achieved by using inexpensive, abundant, and efficient materials, promoting a shift toward more sustainable practices and energy [23].

From the different ES devices in the market and under development, SCs have gained significance in the last decades [24]. SCs, along with Lithium Ion Batteries (LIBs), are among the most promising devices for the energy transition [25]. They are usually used in cases where high currents are needed, but they have low capacitance, and therefore, can only be used for short times. SCs have a greater capacity and can also be recharged without damage, filling the gap between capacitors and conventional batteries [26].

SCs electrodes are mainly based on carbonaceous materials that possess high surface area and appropriate pore-size distribution for the necessary capacitance. Many works are focusing on the development of novel materials with enhanced properties for this application, due to the estimated high demand [27]. Similar to the case of batteries, lignocellulosic materials, especially lignin, are making their way to be considered as a feasible alternative.

The lignins employed in all the works for the development of ES materials are lignosulfonates (LS), or alternatively Kraft lignins. LS have been widely employed due to their appealing properties like water solubility. Nevertheless, its obsolete extraction procedure has resulted in Kraft being the most employed pulping process worldwide. This process generates substantial amounts of KL as waste, which has high potential for valorization. Nonetheless, keeping in mind the utilization and implementation of green processes to obtain more ecological materials, the organosolv method stands out as the most sustainable lignin isolation process. It promotes an integral biorefinery product valorization [28].

However, to the best of our knowledge, no work implementing OL can be found in the literature. Therefore, a novel approach involving the incorporation of OL into AC and the subsequent comparison of these

analogous materials with KL has been carried out. Despite the less sustainable extraction process of KL in comparison to OL, massive quantities of this type of lignin are extracted every year as a side product from paper and pulp industry. Consequently, integrating KL into higher-value products represents a sustainable method for creating innovative advanced materials from waste such as lignin.

Various physicochemical and morphological techniques were used to assess differences in the composition, chemical properties, and morphology of the materials. Fourier Transformed Infrared spectroscopy (FTIR), Elemental Analysis (EA), X-Ray Photoelectron Spectroscopy (XPS), Brunauer–Emmett–Teller (BET) method and Scanning Electron Microscopy (SEM) were utilized for this purpose. Moreover, electrochemical measurements were conducted to determine the materials' electrochemical performance. Cyclic Voltammetry (CV), Electrochemical Impedance Spectroscopy (EIS) and Galvanostatic Charge Discharge (GCD) measurements were performed to study polarization processes, determine specific capacitance values, and gather information about porosity.

2. Materials and methods

2.1. Materials

KL was precipitated from Kraft liquor and OL was extracted from *Eucalyptus globulus* chips, both provided by Papelera Zikuñaga (Hernani, Gipuzkoa) and characterized in a previous work [29]. Granulated activated carbon (7440-44-0, Panreac) was purchased. AC was treated with concentrated nitric acid (HNO_3) (65 %, 7697-37-2, Panreac). N-Methyl-2-pyrrolidone (NMP) (ReagentPlus 99 %, 872-50-4, Sigma-Aldrich) and Poly (vinylidene fluoride) (PVDF) (av. M_w 275,000, 24937-79-9, Aldrich) were used for the slurry preparation, and a glassy carbon sheet (7 mm × 7 mm × 0.5 mm) was used as the current collector of the working electrode. 0.1 M of perchloric acid (HClO_4) in anhydrous acetic acid was used as an electrolyte.

2.2. Treatment of activated carbon

To prepare the TAC, AC was milled and then mixed with concentrated HNO_3 (65 %) until a concentration of 1 g/L was reached. The solution was heated up to 80 °C and stirred at 200 rpm for 2 h. Once the reaction finished, the product was filtered and washed with distilled water through a 0.22 μm nylon filter under vacuum. The obtained product was then dried overnight in an oven at 60 °C.

2.3. Preparation of lignin-activated carbon composites

The surface deposition of KL and OL onto AC and TAC was carried out following the procedure described by Zhou et al. (2019) [23]. Briefly, 200 mg of lignin (KL or OL) and 20 mg of AC or TAC were added to a 40 mL acetone/ H_2O solution (7,3 v/v). Combining all the materials appropriately, the following combinations were obtained: AC-KL, AC-OL, TAC-KL and TAC-OL. The solutions were treated in an US water bath for 15 min. Before filtering, the products were subjected to centrifugation and washed with another 40 mL of the aforementioned acetone/water solution. The resulting filtrate was then sonicated for another 15 min before centrifuging and filtering again. The solid product was dried overnight in an oven at 60 °C.

2.4. Lignin-activated carbon characterization

FTIR spectra analysis was used to determine the oxidation reaction of the AC, and to observe the surface deposition of lignins in both AC and TAC. The spectra were recorded in the range of 4000 to 600 cm^{-1} , with a resolution of 4 cm^{-1} and 64 scans.

For elemental analysis, a Leco TruSpec Micro elemental analyzer was used. 2 mg of sample were heated at 1050 °C. 3× Nippon Gas pure

helium was used as carrier gas and 4× Nippon Gas extra pure oxygen was used as the test gas. Acetanilide (C = 71.09 %, H = 6.71 %, N = 10.36 %, O = 11.84 %) was used for the calibration.

X Ray Photoelectron Spectroscopy (XPS) measurements were carried out in a Versaprobe III Physical Electronics (ULVAC) with Al K α (148.7 eV) monochromatic radiation source. An initial analysis was carried out to determine the elements present (wide scan: step energy 0.2 eV, pass energy 24 eV), followed by the detailed analysis of the detected elements (detail scan: step energy 0.05 eV, pass energy 27 eV, time per step 20 ms) with an electron exit angle of 45°. The spectrometer was previously calibrated with Ag (Ag 3d5/2, 368.26 eV). The spectra were adjusted using the software CasaXPS 2.3.26, which models the contributions after a base subtraction (Shirley). The Gaussian deconvolution of the peaks was carried out by OriginPro 2009.

The surface area and pore characteristics were analyzed by the Brunauer–Emmett–Teller (BET) method. The selected samples were dried at 200 °C for 16 h and measured at 77 K by a nitrogen adsorption-desorption analyzer (Micrometrics ASAP 2420 V2.09). The isotherms were carried out in the range in which the BET equation can be applied for the SSA determination (P/P_0 from 0.01 to 0.4). The used adsorption gas was nitrogen, and the set temperature was 77.3 K.

SEM images were recorded with a Hitachi S-4800 FEG-SEM operating at an accelerating voltage of 5 kV. Samples were previously coated with a 15 nm gold layer in an Emitech K550x ion sputter.

2.5. Electrochemical characterization

30 mg of the composite material were dissolved in 250 μ L of NMP (10 % dry mass of PVDF). The solution was stirred until its complete dissolution and 10 μ L were poured into a glassy carbon membrane ($7 \times 7 \times 0.5$ mm), used as a current collector, and dried at 60 °C overnight.

The electrochemical behavior of the designed materials was analyzed by CV and EIS. A BioLogic VSP potentiostat/galvanostat and a three-electrode system composed of Ag/AgCl (KCl 3.5 M) as a reference electrode (RE) and Pt wire as the counter electrode (CE) were employed. The composite material was deposited in the current collector and fixed in a tantalum clip as a working electrode (WE) and 0.1 M HClO $_4$ was used as electrolyte.

CV measurements were carried out from -0.2 to 0.8 V at different scan rates (5, 10, 15, 20, 25, and 50 $\text{mV}\cdot\text{s}^{-1}$), both pre- and post-GCD. The CV cycles obtained were used for the capacity determination, using the absolute value of their integration as the area value in the following Eq. (1):

$$C_p = \frac{A}{2mk\Delta V} \quad (1)$$

where C_p is the capacity (F/g), A is the area of the CV curve (A V), m is the mass of the active material (g), k is the scan rate (V/s) and ΔV is the voltage range (V).

EIS measurements were performed from 1 MHz to 10 mHz, both pre- and post-GCD. Each experiment was divided into four sequences: very high (from 1 MHz to 100 KHz), high (from 100 KHz to 10 KHz), intermediate (from 10 KHz to 100 Hz), and low (from 100 Hz to 10 mHz), with 6, 10, 20, and 31 points per decade respectively. Once the impedance spectra were obtained, the data was processed through Matlab R2022a and the DRTtools extension to obtain the Distribution of the Relaxation Time (DRT) graphs, which were useful for the identification of the elements and design of the Equivalent Circuit Models (ECM). The ECM design was introduced in the EC-Lab software and fitted to the experimental Nyquist plot using Zfit. Once a proper fit was obtained, the values of each of the elements conforming to the ECM were recorded. Moreover, the porosity characteristics of the sample were also observed by the Bode plots.

Galvanostatic charge/discharge (GCD) cycles were also performed to observe the durability of the materials and measure the C_p of each cycle

at different current densities (I_m). Three different current densities ranging from 0.2 to 5 A/g were used, and 100 cycles of charge and discharge were carried out in the potential range of -0.2 and 0.8 V. The specific capacitance of selected cycles was calculated by the following Eq. (2):

$$C_p = \frac{I_m \cdot \Delta t}{\Delta V} \quad (2)$$

where C_p is the capacity (F/g), I_m is the current density (A/g), Δt is the time range of discharge (s) and ΔV is the potential range of the discharge (V) [11,30].

3. Results and discussion

3.1. Chemical composition

The chemical composition of AC, TAC, and the composites were determined by FTIR and EA, shown in Fig. 1. The main difference between the spectra of AC and TAC was the increase of the C=O and C–N stretching bands in TAC, at 1700 and 1100 cm^{-1} respectively. This was due to the treatment with concentrated HNO $_3$, which is a strong oxidizing agent that react with carbon yielding oxidized carbon with different structure and properties. The main functional groups are the carboxyl (-COOH), carbonyl (-C=O) and nitro (-NO $_2$) groups, whose associated bands were observed to have increased in the FTIR analysis [31].

This first band at 1700 cm^{-1} also increased with the insertion of both KL and OL. Moreover, the band associated with O–H stretching, at 3400 cm^{-1} , also augmented when AC and TAC were treated with the lignins, along with C=O stretching at 1700 cm^{-1} , COO $^-$ stretching at 1620 cm^{-1} , and C–O–C stretching at 1200 cm^{-1} [23,32,33]. It can be concluded that the spectra verify both the oxidation of activated carbon by the reaction with HNO $_3$ and the insertion of lignin particles onto the surface of the carbon by US treatment due the increment of the bands associated with lignin in the composite spectra.

Results obtained from EA are shown in Fig. 1 (right). The main elements composing these materials were quantified (C, H, N, S, and O) and used for oxidation treatment and lignin deposition verification. It can be observed that AC was composed mainly of C, with almost 90 % of the total composition, followed by O, with a little over 10 % of the total composition. The other elements found (N, H and S) were minor. After the treatment with HNO $_3$, it can be seen that oxygen content considerably increased to over 30 % of the total composition, results that match with the ones obtained in other works [34]. N content also increased, due to the insertion of N functional groups into the surface, as verified by FTIR spectra. With the deposition of KL and OL into the AC surface, some other changes in the composition can also be observed. In the case of AC-KL, sulfur content considerably increased, due to the sulfur functional groups present in KL, resulting from the lignin isolation process carried out in the industry. H content also showed a slight increase, although it was less noticeable, considering lignin's predominantly carbonaceous composition. Lignin, however, had a higher H content than AC. A similar trend can be observed with OL, but without the increase in S content, as

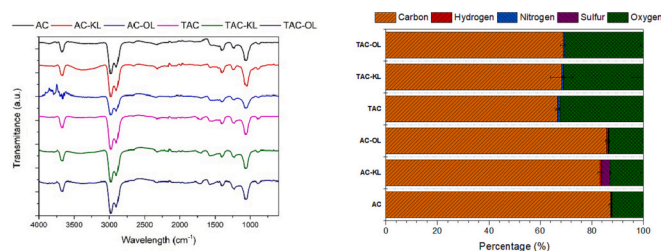


Fig. 1. FTIR spectra (left) and EA (right) of AC, AC-KL, AC-OL, TAC, TAC-KL, and TAC-OL.

the isolation of organosolv lignin does not imply the use of sulfur compounds. The introduction of KL and OL onto the TAC particles did not result in significant differences, since the C, O, and N content remained relatively similar. Nevertheless, the overall changes in the composites' composition were confirmed by EA.

Quantitative XPS analysis was carried out to verify the results obtained from FTIR and EIS, as well as to observe the different linkages present in the surface of the samples. Table 1 shows the atomic composition of the selected samples, while Fig. 2 depicts the XPS surveys. It can be observed that AC was mainly composed of C atoms, a proportion that diminished after acid treatment and further decreased with lignin deposition. C content decreased from 88.2 % to 78.8 % and 67.6 % respectively, almost proportionally increasing the O content. Although the results are in concordance with the ones obtained in EA, a higher proportion of O was obtained with XPS. This is due to the higher amount of lignin present in the surface, as analyzed by XPS, rather than the whole sample, which was analyzed by EA.

In terms of the differences in linkages, C 1s and O 1s linkages are depicted and deconvoluted in Figs. A1 and A2. As a consequence of the reduced C content, the intensity of the C 1s peak decreased throughout the process. The peak attributed to the O-C=O linkage at 288 eV remained similar in all samples. However, the presence of the C-O-C linkage (at 286 eV) increased with the acid-treatment and the subsequent OL deposition, reaching proportions similar to those of C-C (at 284 eV) and C-O-C linkages [35].

On the other hand, the O 1s spectra shown in Fig. A2 showed a corresponding increase in intensity due to its higher presence. AC sample displayed an O 1s peak that belonged almost completely to the C-OH linkage at 533 eV, with a minimum presence of C=O at 530 eV. Both of these peaks increased their intensity in TAC, particularly with a more considerable presence of C=O. However, upon the incorporation of OL, this functional group slightly decreased, probably due to new linkages formed between TAC and OL, leading to a vast increase in C-OH linkage. This presence more than doubled compared to the initial AC sample. Additionally, the incorporation of the new COOH linkage at 534 eV occurred [36]. These two linkages are very common in lignin molecules, which confirms the successful deposition of lignin on TAC surface.

3.1.1. Morphology

The adsorption isotherms obtained at the very low relative pressures were recorded and shown in Fig. 3. The results revealed that the N₂ adsorbed at the lowest P/P₀ happened at the smallest pores. The higher value of adsorption indicated that the surface of the sample had more pores, suggesting that the specific surface area was higher. It can be observed that the treatments were effective on increasing the SSA, as the values increased from 839.6794 m²/g for the AC sample, to 969.9886 m²/g for the TAC treated with HNO₃ and further to 1103.6504 m²/g for TAC-OL.

The surface morphology of the samples was further observed by SEM imaging. Three images in different scales were obtained for each material type. Fig. 4 shows the images obtained at 2 μm scale, and Figs. A3 and A4 show the images at 5 μm and 20 μm scales respectively. It can be observed that the surface of the activated carbon became rougher after the treatment with HNO₃. Moreover, with the deposition of KL and OL onto the surface of AC and TAC, a considerable increase in the porosity degree can be observed. In AC-KL sample, large macropores with a width

Table 1

The chemical composition (atomic %) of the surface of the selected samples (AC, TAC and TAC-OL) measured by quantitative XPS.

Sample	C	O	N ^a	Si ^a
AC	88.2	11.3		0.5
TAC	78.8	19.5	0.8	0.8
TAC-OL	67.6	31.9		0.6

^a Estimated value, near-noise spectra.

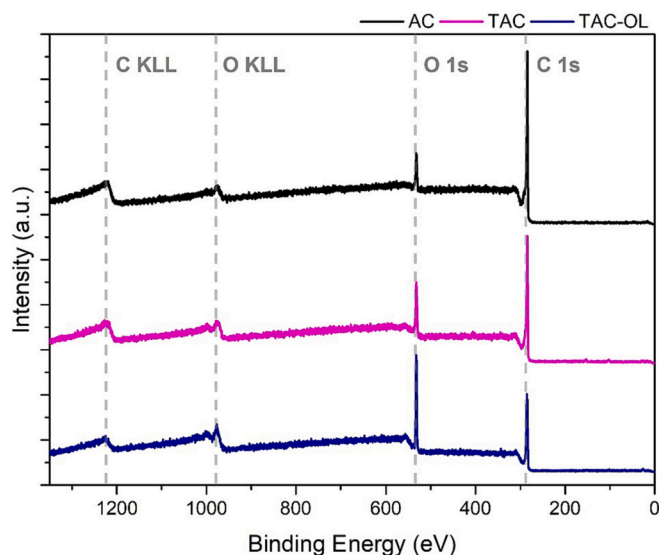


Fig. 2. XPS of the selected samples (AC, TAC and TAC-OL).

of approximately 0.5 μm were observable, along with much smaller pores that had mesoporous widths, spread through the material. In the case of TAC-KL, much smaller pores were obtained, with an overall 0.1 μm width value for the biggest pores, but also with a presence of much smaller pores. Compared to the other samples, AC-KL, TAC and AC, the SSA had drastically increased in TAC-KL, creating innumerable pores and cavities that are expected to enhance further ion transportation and adsorption. Sample AC-KL and AC-OL had similar morphology, implying that the type of lignin did not considerably affect the structure of the hybrid material obtained. However, in the case of TAC-KL and TAC-OL, more differences can be observed, since the pores obtained at TAC-OL were considerably smaller than for TAC-KL. This might be beneficial for the application for which is designed, having more meso- and micropores, and optimizing the ion diffusion. In Table A2, average porosity sizes obtained from 10 measurements using the software Image J are listed.

3.1.2. Electrochemical characterization

The composite materials obtained were used as working electrodes in a three-electrode system, where Ag/AgCl served as RE and Pt as CE, using 0.1 M HClO₄ as the electrolyte. CV and EIS measurements were carried out before and after galvanostatic cycling to observe the differences caused in the materials and deduce their stability and enhancement in performance. The CV cycles obtained are shown in Fig. A5 and the Nyquist plots obtained from the EIS are depicted in Fig. 5. From these measurements, different polarization processes were identified. Curve fitting using ECMs was carried out, specific capacitance values were obtained, and porosity structures were deduced.

To analyze the EIS spectra obtained with the EC-Lab Software, it is essential to design an ECM that accurately represents the different polarization processes occurring in the system. This approach ensures obtaining values that align with the experimental data. This was done by the distribution of relaxation time (DRT) methodology [37–41]. EIS data were deconvoluted and the Z_{real} and Z_{imag} impedance data were converted to gamma tau (γ(τ)/Ω) and relaxation times (τ/s) by the use of Matlab and DRTtools toolbox [42,43]. The DRT graphs obtained before GCD (called pre-GCD) and after GCD (called post-GCD) for each sample are illustrated in Fig. A3, and the most significant results are presented in Fig. 6. All the polarization processes taking part in the system were observed, and differences made by both composition and the charge and discharge cycles were deduced. Moreover, the frequency ranges were distinguished and the elements composing the ECM were assigned to the corresponding frequency range. Depending on the sample, two types of

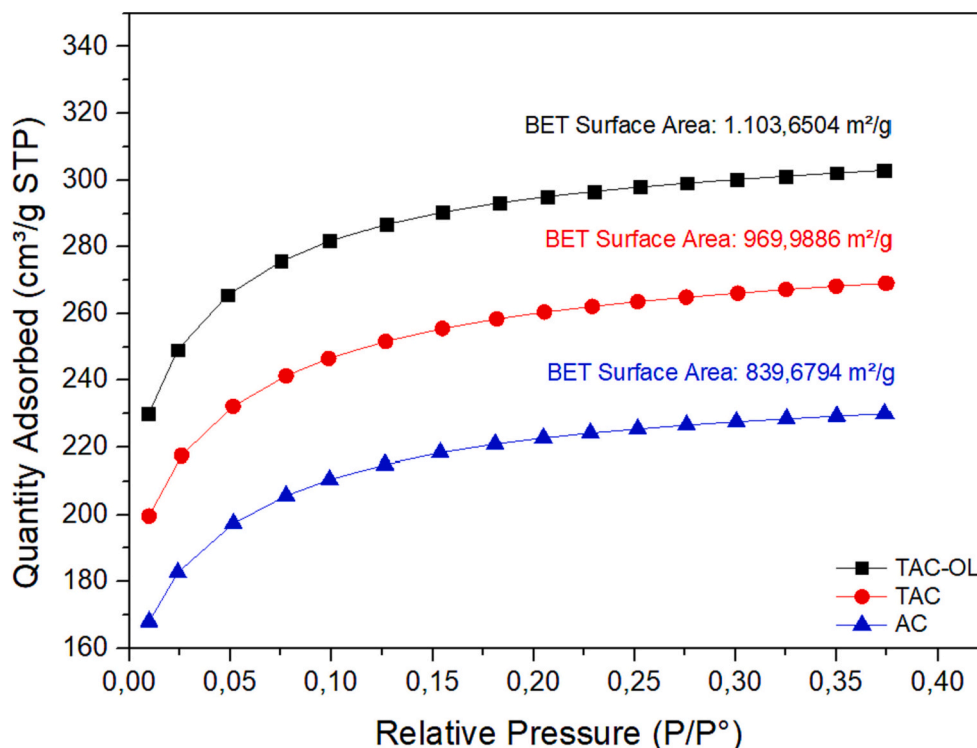


Fig. 3. Low pressure nitrogen adsorption isotherms of the selected samples (AC, TAC and TAC-OL).

polarization responses could be observed. Most of the composite materials showed polarization processes through all the frequency ranges, while in the case of TAC and TAC-KL, the main polarization processes occurred between the low and high frequencies. Depending on that, two different ECM were designed. Each observed polarization process was attributed to an element couple (CPE and R), except for the polarization processes happening at low frequencies, which were attributed to diffusion processes taken into account as the Warburg element (W_d). The DRT graph of TAC-KL in Fig. 6 also shows the zoomed-in values at high frequencies. However, due to the huge difference in the values compared to the W_d obtained, the polarization processes happening at very high frequencies can be neglected.

As previously mentioned, the relaxation times for the DRT graphs were obtained by converting the frequency values. Therefore, it can be concluded that relaxation times ranging from 10^{-8} to 10^{-4} s (colored in blue) were attributed to polarization processes happening at very high frequencies (1 MHz to 100 KHz). Time intervals from 10^{-4} to 10^{-2} s (colored in red) were attributed to high frequencies (100 KHz to 10 KHz), intervals from 10^{-2} to 10^1 s (colored in green) were linked to intermediate frequencies (10 KHz to 100 Hz), and finally, intervals from 10^1 to 10^4 s (colored in purple) were attributed to low frequencies (100 Hz to 10 mHz).

Based on the results, two different ECMs were designed and presented in Fig. 7. The ECM model on top, with 3 CPE and R couples corresponds to the samples showing polarization processes at very high frequencies: AC, AC-KL, AC-OL, and TAC-OL samples. Otherwise, the ECM model below, with 2 couples, corresponds to the samples TAC and TAC-KL. These models were introduced in the EC-Lab software and fitted to the Nyquist plots experimentally obtained.

L1 and R1 were attached in series; L1 corresponded to external elements like cables or connections, while R1 was the resistance that the electrolyte (in this case 0.1 M $HClO_4$) created in the system. There were another three groups of elements linked in parallel (CPE2 and R2, CPE3 and R3, and CPE4 and R4). The first one corresponded to the highest frequency range (from 1 MHz to 100 KHz), with a polarization process happening at $\tau = 10^{-6}$ s, in the most external part of our samples

employed as a working electrode. CPE3 and R3 were in the high-frequency area (from 100 MHz to 10 KHz), with polarization processes occurring at 10^{-2} s. The last elements in parallel (the CPE4 and R4) were in intermediate frequencies (from 10 KHz to 100 Hz), in a more internal area of the material, where charge transfer phenomena occur. Finally, the low-frequency area (from 100 Hz to 10 mHz) is where diffusion processes occur, and as can be seen from the DRT graphs obtained, two elements took part in that frequency range. The first one, at around 50 s, was assigned to the Warburg element (W_d) and the second one, at around 100 s, was another C element (C1), which would be attached in series to the ECM [44,45].

The other ECM that fits the Nyquist plots obtained for TAC and TAC-KL samples was also composed of the elements L1 and R1 in the series. Nevertheless, this time only two C and R couples in parallel were observed (CPE2 and R2 in the high-frequency range and CPE3 and R3 in the intermediate range). Similarly, the Warburg element corresponded to the diffusion processes happening in the low-frequency range, with a final C element. From the left graph of Fig. 6, it can be observed that the polarization processes at high frequencies were so low compared to the ones obtained at low frequencies, that the elements that would correspond to $\tau_{\text{very high}}$ are neglected for the ECM. Moreover, to compare the C_p obtained from EIS with the ones of CV, only the elements presented at low frequencies were considered since the CV measurements were carried out at constant tension and current.

The fits obtained for the samples TAC-KL and TAC-OL are shown in Figs. A8 and A9. It can be observed that both Nyquist plots exhibited different linearity. Consequently, the corresponding DRT graph also differed significantly, and different ECM were needed for an accurate fit.

In terms of changes observed due to the galvanostatic cyclings, some minor changes in the diffusion processes were observed. Some peaks showed a shift in the relaxation time, while other elements showed a considerable value change, especially at low frequencies. The values obtained for all the elements of the ECMs identified are listed in Table A3 for pre-GCD values and Table A4 for post-GCD values. AC samples showed quite pronounced polarization processes through all the frequencies. AC-KL, AC-OL, and TAC-OL samples also showed

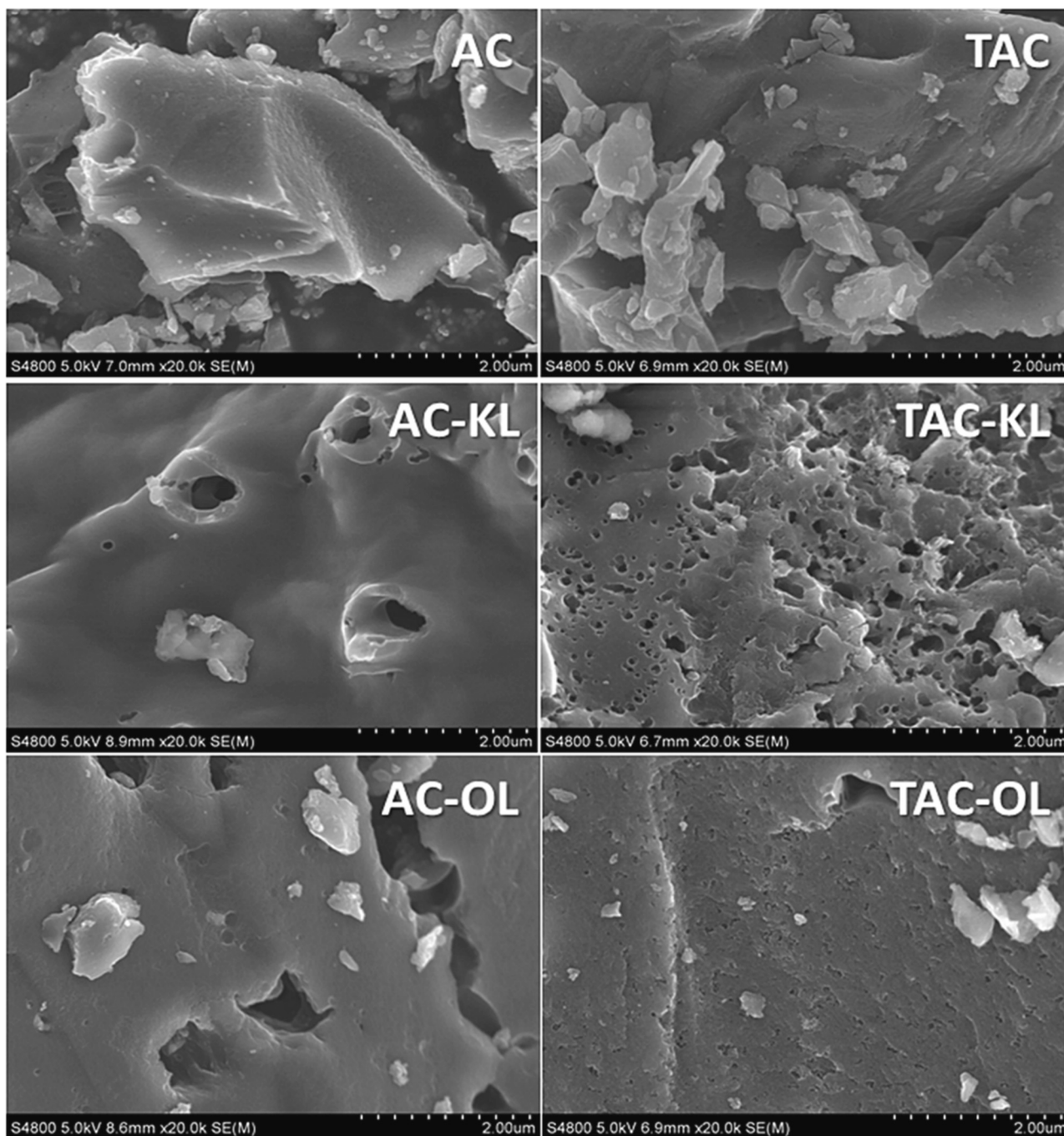


Fig. 4. SEM images of AC, AC-KL, AC-OL, TAC, TAC-KL, and TAC-OL at 2 μm scale.

pronounced processes, especially at intermediate frequencies. In the case of TAC and TAC-KL, since the peaks at low frequencies were so high, other polarization processes were not so visible. However, they still had higher values than the other types of materials (AC had a value of 460 Ω at 1 s, while TAC had a value of 1153 Ω and TAC-KL 490 at the same time). Values corresponding to the diffusion processes are the ones that should be observed more precisely. AC showed similar polarization processes pre-GCD and post-GCD at low frequencies (around 1000 Ω between 50 s and 100 s), similar to TAC-OL. It can therefore be concluded that these are the most stable samples since no significant changes could be observed by the GCD cyclings. In the case of AC-KL and TAC-KL, GCD cycles decreased the diffusion processes. In the case of AC-KL, the values at 34 s decreased from 2500 to 720 Ω , and from 1500 to 400 Ω at 100 s, while for TAC-KL values at 40 s decreased from 43,300 to

2570 Ω , and from 33,000 to 14,100 Ω at 100 s. The only sample that shifted diffusion times was AC-OL, where the main time fluctuated from 37 s to 9 s.

Specific capacitance values were obtained by CV, EIS and GCD data. EIS C_p values were calculated using the PseudoC tool of the EC-Lab, equivalent value to the CPE value obtained from the ECM. On the other hand, C_p values obtained from CV, were calculated using Eq. (1), where the total area value of the CV cycles obtained was introduced for the calculations. Six different scan rates were performed for each sample (5, 10, 15, 20, 25, and 50 mV/s), and 5 cycles were carried out for each scan rate. The mean values and errors of the capacitance values calculated are illustrated in Fig. A5. It can be observed that lower scan rates showed the highest capacitance values for most of the samples, values that decreased as the scan rates increased, obtaining the smallest values

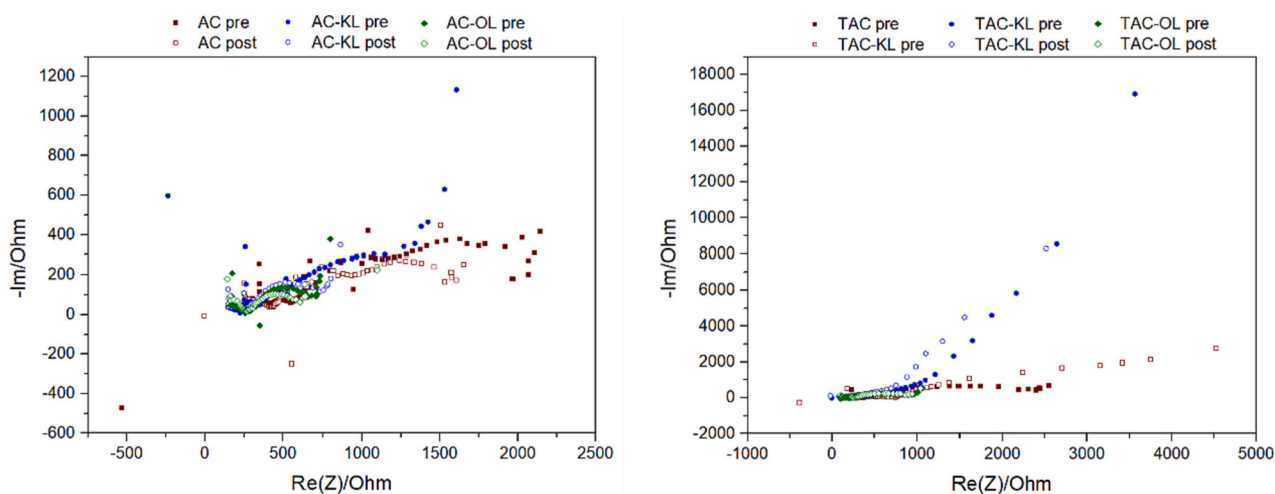


Fig. 5. Nyquist plots of all the samples.

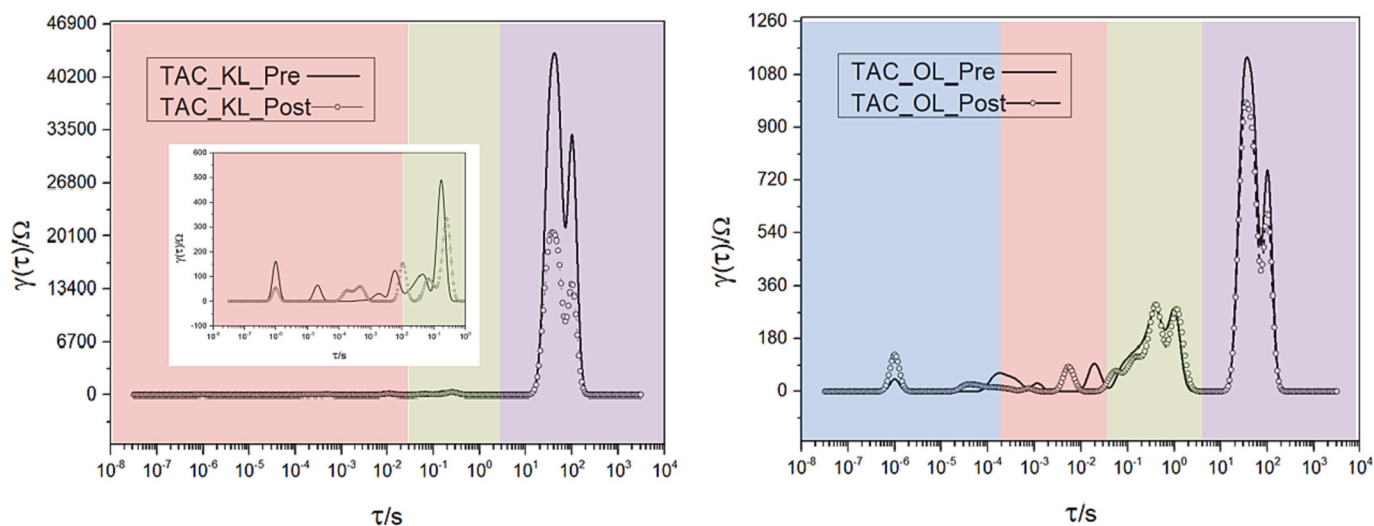


Fig. 6. DRT graphs of TAC-KL and TAC-OL samples.

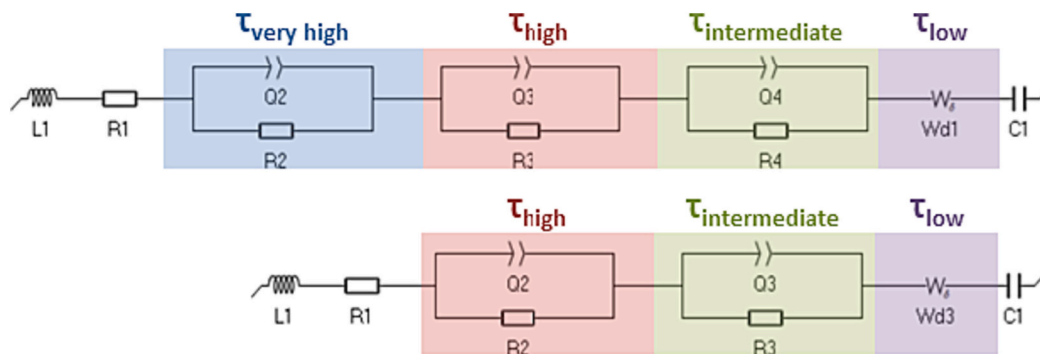


Fig. 7. ECM of the different samples.

at 50 mV/s. Other works also showed a decrease in capacitance values with higher scan rates [46]. The influence of the scan rate on the capacitance obtained can be useful to determine the electrochemical charge storage mechanism of the active material. There are three types: electric double-layer capacitors (EDLC), pseudocapacitors (PS), and batteries. Faradaic processes happen in the first two types, and these reactions are surface-controlled. Meanwhile, the third type is generated

by non-Faradaic processes, controlled by diffusion mechanisms. Consequently, the kinetics of these processes are also different. To identify the type of process, Eq. (3) can be applied:

$$i = a \cdot \nu^b \tag{3}$$

where i is the current, a and b are constants, and ν is the scan rate.

The b value reflects the kinetics of the reaction. When b equals 1.0 means that the process is surface-limited, and if b is 0.5 it means that the main phenomenon happening is a diffusion-controlled redox reaction [47]. From the lines obtained in Fig. 8, the active materials showed an EDLC or PC behavior. This suggests that charges accumulated at the electrode-electrolyte interface creating electrostatic charges without redox reactions. Nevertheless, in the cases of samples TAC-KL and TAC-OL, as compared to TAC, there was a significant decrease in the b value, a value of 0.5, especially in the case of TAC-OL. This indicates that the addition of lignin particles onto the surface led to redox reactions, slightly changing the behavior of the active material [47].

As mentioned before, CV, EIS and GCD were used to calculate the capacitance values. These electroanalytical tests are complementary. In CV, the faradaic response generated (as a form of current) is measured by the difference of potential, scanned from one potential to another, and reversed back to the initial potential. In EIS, a specific AC potential is applied at different frequencies and in a specific amplitude, and the impedance change is measured, composed of resistive, capacitive and inductive phenomena. Finally, the GCD technique charges and discharges the active material in a certain amplitude, measuring the time it takes for each charge and discharge, dependent on the current density applied. Therefore, the bases of the measurements are different. While the CV measures the capacitive behavior at a specific frequency, EIS measurements are frequency-dependent, and GCD cyclings current density dependent. Moreover, the composition, surface area and porosity can influence the response given by different electrochemical stimuli, obtaining variations in the capacitive values obtained. Generally, CV measurements are more suitable for capturing fast surface processes, while EIS measurements can identify slow diffusion and charge transfer processes more efficiently. Having those limitations in mind, a proper electrochemical characterization of the materials can be obtained [48].

The data obtained by the CV measurements at different scan rates were used to calculate the C_p (CV), by applying the previously mentioned Eq. (1). Additionally, the C_p (EIS) values were obtained by fitting the Nyquist plots to the corresponding ECM, and finally, the C_p (GCD) at different current densities were obtained by applying the Eq. (3). The C_p values obtained from all three electrochemical techniques are listed in Table A5 and compared in Fig. 9. The correlation of the values was carried out between the conditions in which the most similar values were obtained, low scan rate of 5 mV/s for the CV and medium-high current of 3 A for GCD measurements.

The results show that the insertion of KL and OL particles onto the surface of the AC had a positive effect on the performance of the material

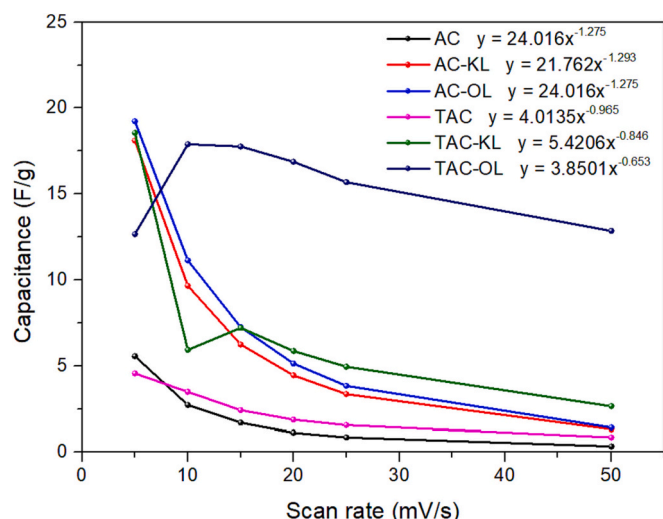


Fig. 8. Capacitance values (F/g) of different materials with different loadings.

in terms of capacitance. C_p values obtained by CV (C_p (CV)) fluctuated from around 5 F/g for AC to almost 20 F/g for both AC-KL and AC-OL, with no detrimental effect due to the galvanostatic cycling. A similar effect could be observed with the TAC composites, where the insertion of KL and OL also favored both pre- and post- C_p (CV) values. In terms of the values obtained by EIS (C_p (EIS)), an overall similar tendency could be observed but with some differences. Composites usually show a better performance, but in this case, the ones that were conformed with OL, both AC-OL, and TAC-OL exhibited the best results. Their C_p experienced a significant increase both pre- and post-GCD cycles, with enhanced performance after the cycles. Nevertheless, the results obtained from the GCD differ slightly. The insertion of KL and OL into AC resulted in a negative effect compared to the value of AC, while TAC-KL showed similar results to TAC, and TAC-OL higher values than the TAC analogue. As explained above, the differences observed between the techniques can be attributed to the basis of the measurements. The overall C_p (CV) values are considerably lower than the C_p (EIS), probably due to the conductivity mechanism that the synthesized materials have, which is likely to be based primarily in diffusion processes.

A characteristic closely related to the capacity of the material is its porosity. The pore size (mesoporous or microporous) dictates the electrolyte penetration and its overall performance [33,45]. Mesopores enable a fast power delivery due to the low ion resistance while micropore structures are more appropriate for high energy density. Therefore, a way to reach both, fast power and high energy density is by obtaining an electrode material with micro-, meso-, and macro-pores [45]. These morphological characteristics were analyzed by SEM, which confirmed that the AC treatment and addition of lignin to the material were beneficial for a hierarchical pore structure. In addition, this property was further analyzed and confirmed by EIS analysis.

Although the ECM obtained from the EIS data was useful to obtain C_p values, it was not able to express phenomenological information derived from the surface structure of the material. The polarization processes, along with their corresponding relaxation times, are linked to the CPE-R couple operating in that frequency range. Consequently, this relationship provides insights into the layer in which the material (inner or outer) is functioning within that frequency domain. From that CPE-R couple, the equivalent specific capacitance is obtained, which is therefore linked to the porosity of the material and the ease with which it accepts charge and discharge [45].

Mesopores (2–50 nm) provide low resistive ion transport pathways essential for fast power delivery, while the micropores (<2 nm) provide higher specific surface area essential for high energy density. Moreover, the length of these pores and the surface heterogeneity will also depend on the specific capacitance obtained [20,49,50]. To observe the porosity effect on the EIS results, impedance modulus ($\text{Log}|Z|(\Omega\text{cm}^2)$) and impedance phase angles ($\varphi(^{\circ})$) were plotted against the frequency. The graphs for each sample were plotted and can be seen in Fig. A6, and the most significant results (for samples TAC-KL and TAC-OL) are in Fig. 8.

Since micro- or meso-pores show different resistance, the peak associated with each in $\text{Log}|Z|$ vs $\text{Log } \nu$ appear in different frequencies. Micropores show higher resistance due to their smaller size, so they appear at lower frequencies, while mesopores, being bigger, are visible at higher frequencies. Structures with both pore types show two peaks at different frequencies. From Fig. A9 it is evident that the processes carried out contributed to the formation of both micro- and meso-pores. AC sample did not show any significant peak across various frequencies. In contrast, TAC displayed a clear peak in the micropore area and another smaller but clear peak in the mesopore area. When hybrid or composite materials were obtained with the lignin insertion, slight differences were observed. The deposition of KL, especially, enhanced mesopore formation in untreated AC (AC-KL). This was corroborated with the results obtained from SEM, where big pores were observed.

In the case of OL deposited in AC (AC-OL), the micropore response observed was the most significant among all the samples analyzed. For composites obtained from treated AC, similar impedance responses were

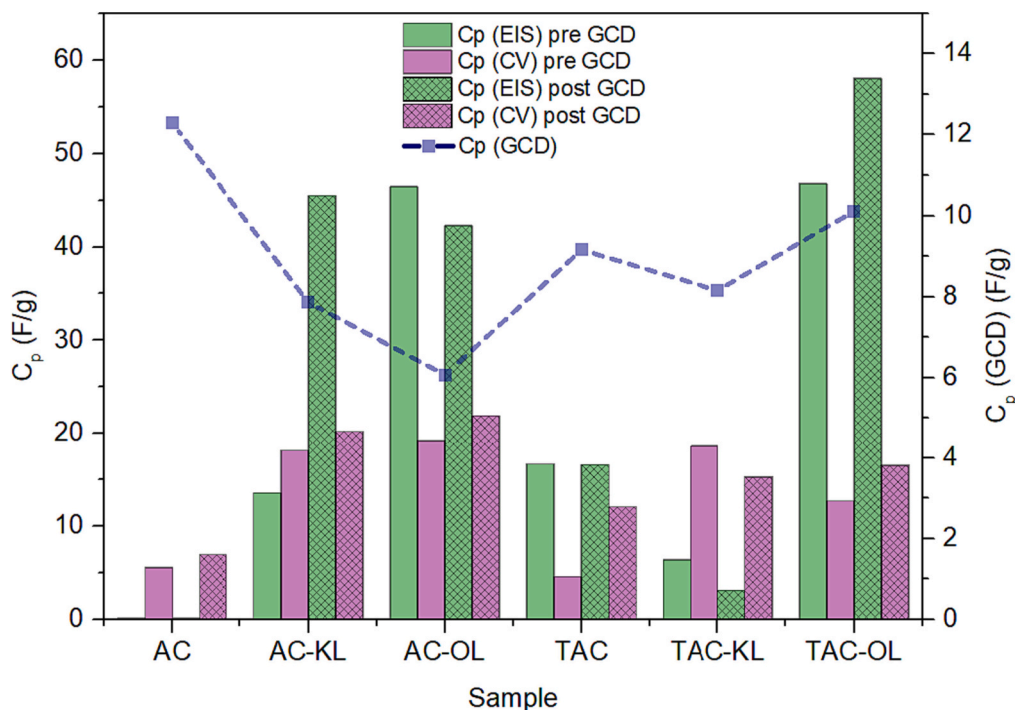


Fig. 9. Comparison of C_p values (F/g) calculated by the different electrochemical measurements (CV, EIS and GCD).

observed for all TAC, TAC-KL, and TAC-OL, where slight micropore responses were seen, and a more significant mesopore response. Nevertheless, a common difference between TAC-OL from TAC and TAC-KL was that the micropore response happened at lower frequencies. This suggests the potential formation of smaller micropores and a higher energy density material. Once again, SEM images supported this observation, where TAC-OL showed significantly smaller pores than TAC-KL (Fig. 10).

4. Conclusions

The aim of the work was to obtain composite materials with improved performance to use as electrode active material in SCs. The research involved treating AC with HNO_3 to assess if the chemical reaction promoted the increase in both functional groups and insertion of lignin particles. This effect was confirmed through FTIR and EA,

demonstrating the effectiveness of the treatment.

Moreover, the type of lignin used considerably affected the resulting porous material obtained, creating a more hierarchically porous surface when KL was deposited in TAC, while a more mesoporous structure was obtained when OL was deposited in TAC. This last morphology was found to be the most electrochemically efficient, leading to the highest C_p values.

The porous structures of the composite materials were thoroughly analyzed by SEM and EIS. The C_p values obtained by CV, EIS and GCD electroanalytical tests were compared, revealing notable differences between them, and emphasizing the complexity of the electrochemical behavior of the composite material. This analysis led to the conclusion that the conductive mechanism of the materials synthesized relied mostly on diffusion processes.

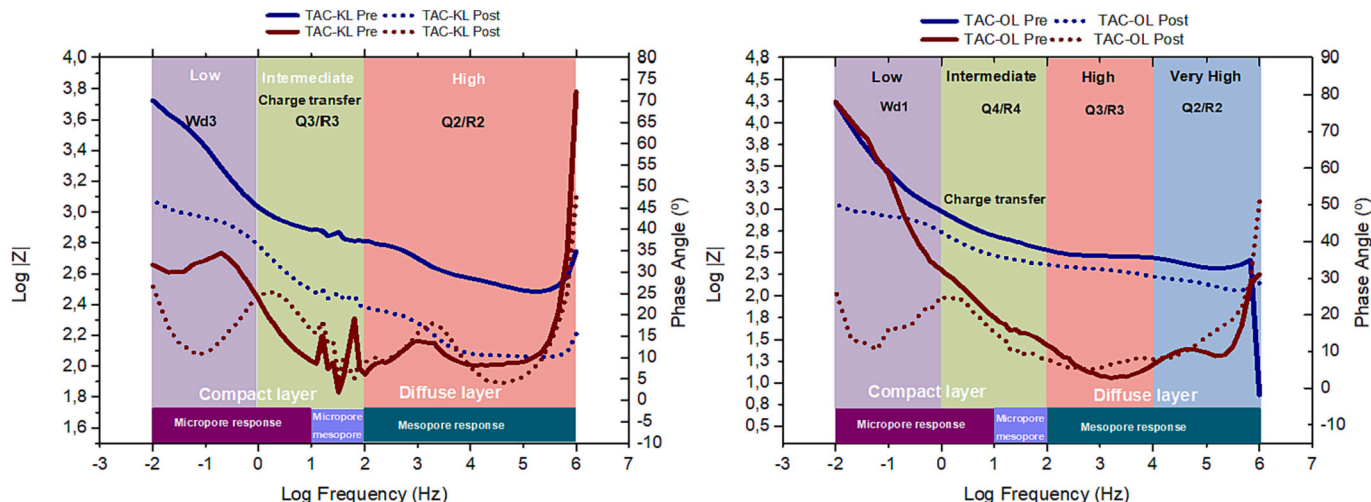


Fig. 10. Bode plots of TAC-KL and TAC-OL.

CRedit authorship contribution statement

Nagore Izaguirre: Conceptualization, Data curation, Formal analysis, Investigation, Methodology, Visualization, Writing – original draft. **Mikel Alberro:** Conceptualization, Data curation, Formal analysis, Visualization, Writing – original draft. **Xabier Erdocia:** Conceptualization, Methodology, Supervision, Validation, Writing – review & editing. **Jalel Labidi:** Funding acquisition, Resources, Supervision, Writing – review & editing.

Declaration of competing interest

The authors declare the following financial interests/personal relationships which may be considered as potential competing interests: Jalel Labidi reports financial support was provided by Diputación Foral de Guipuzcoa. Nagore Izaguirre reports financial support was provided by Basque Government.

Data availability

Data will be made available on request.

Acknowledgements

The authors would like to acknowledge the Basque Government for the financial support of this research through project IT1498-22 and grant PIF19-183). The authors thank for the technical and human support provided by SGiker (UPV/EHU/ERDF, EU), European financial support (FEDER and FSE), and Texture Laboratory of the Scientific and Technical Service of INCAR-CSIC.

Appendix A. Supplementary data

Supplementary data to this article can be found online at <https://doi.org/10.1016/j.est.2023.110386>.

References

- J.L. Espinoza-Acosta, P.I. Torres-Chávez, J.L. Olmedo-Martínez, A. Vega-rios, S. Flores-gallardo, E.A. Zaragoza-Contreras, Lignin in storage and renewable energy applications: a review, *J. Energy Chem.* 27 (2018) 1422–1438, <https://doi.org/10.1016/j.jechem.2018.02.015>.
- W.-J. Chen, C.-X. Zhao, B.-Q. Li, T.-Q. Yuan, Q. Zhang, Lignin-derived materials and their applications in rechargeable batteries, *Green Chem.* (2022) 565–584, <https://doi.org/10.1039/d1gc02872c>.
- K. Zhang, M. Liu, T. Zhang, X. Min, Z. Wang, L. Chai, Y. Shi, High-performance supercapacitor energy storage using a carbon material derived from lignin by bacterial activation before carbonization, *J. Mater. Chem. A* 7 (2019) 26838–26848, <https://doi.org/10.1039/c9ta04369a>.
- Y. Tong, J. Yang, J. Li, Z. Cong, L. Wei, M. Liu, S. Zhai, K. Wang, Q. An, Lignin-derived electrode materials for supercapacitor applications: progress and perspectives, *J. Mater. Chem. A* 11 (2022) 1061–1082, <https://doi.org/10.1039/d2ta07203c>.
- C. Xiong, M. Li, S. Nie, W. Dang, W. Zhao, L. Dai, Y. Ni, Non-carbonized porous lignin-free wood as an effective scaffold to fabricate lignin-free Wood@Polyaniline supercapacitor material for renewable energy storage application, *J. Power Sources* 471 (2020) 228448, <https://doi.org/10.1016/j.jpowsour.2020.228448>.
- H. Liu, T. Xu, K. Liu, M. Zhang, W. Liu, H. Li, H. Du, C. Si, Lignin-based electrodes for energy storage application, *Ind. Crops Prod.* 165 (2021), <https://doi.org/10.1016/j.indcrop.2021.113425>.
- H. Wang, F. Fu, M. Huang, Y. Feng, D. Han, Y. Xi, W. Xiong, D. Yang, L. Niu, Lignin-based materials for electrochemical energy storage devices, *Nano Mater. Sci.* (2022), <https://doi.org/10.1016/j.nanoms.2022.01.002>.
- L. Wang, T. Morishita, M. Toyoda, M. Inagaki, Asymmetric electric double layer capacitors using carbon electrodes with different pore size distributions, *Electrochim. Acta* 53 (2007) 882–886, <https://doi.org/10.1016/j.electacta.2007.07.069>.
- A. Srivastava, B. Gupta, A. Majumder, A.K. Gupta, S.K. Nimbhorkar, A comprehensive review on the synthesis, performance, modifications, and regeneration of activated carbon for the adsorptive removal of various water pollutants, *J. Environ. Chem. Eng.* 9 (2021) 106177, <https://doi.org/10.1016/j.jece.2021.106177>.
- A. Bello, J. Dangbegnon, D.Y. Momodu, F.O. Ochai-Ejeh, K.O. Oyedotun, N. Manyala, Green and scalable synthesis of 3D porous carbons microstructures as electrode materials for high rate capability supercapacitors, *RSC Adv.* 8 (2018) 40950–40961, <https://doi.org/10.1039/C8RA08534J>.
- M. Bilal, K. Landskron, Activated carbon electrodes with enhanced supercapacitive swing adsorption of carbon dioxide, in: *ECS Meet. Abstr.* MA2023-01, 2023, p. 2683, <https://doi.org/10.1149/ma2023-01552683mtgabs>.
- M. Forouzeh, A. Ebadi, A. Aghaeinejad-Meybodi, R. Khoshbouy, Transformation of persulfate to free sulfate radical over granular activated carbon: effect of acidic oxygen functional groups, *Chem. Eng. J.* 374 (2019) 965–974, <https://doi.org/10.1016/j.cej.2019.05.220>.
- W. Zhu, X. Zhang, Y. Yin, Y. Qin, J. Zhang, Q. Wang, In-situ electrochemical activation of carbon fiber paper for the highly efficient electroreduction of concentrated nitric acid, *Electrochim. Acta* 291 (2018) 328–334, <https://doi.org/10.1016/j.electacta.2018.08.127>.
- S. Veeresh, H. Ganesha, Y.S. Nagaraj, H. Devendrappa, Structural, morphological characterization of nitric acid and potassium hydroxide activated carbon composite, *Mater. Today Proc.* (2023), <https://doi.org/10.1016/j.matpr.2023.06.156>.
- J.P. Chen, S. Wu, Acid/base-treated activated carbons: characterization of functional groups and metal adsorptive properties, *Langmuir* 20 (2004) 2233–2242, <https://doi.org/10.1021/la0348463>.
- J. Choma, W. Burakiewicz-Mortka, M. Jaroniec, Z. Li, J. Klinik, Monitoring changes in surface and structural properties of porous carbons modified by different oxidizing agents, *J. Colloid Interface Sci.* 214 (1999) 438–446, <https://doi.org/10.1006/jcis.1999.6246>.
- J.W. Shim, S.J. Park, S.K. Ryu, Effect of modification with HNO₃ and NaOH on metal adsorption by pitch-based activated carbon fibers, *Carbon N. Y.* 39 (2001) 1635–1642, [https://doi.org/10.1016/S0008-6223\(00\)00290-6](https://doi.org/10.1016/S0008-6223(00)00290-6).
- H.P. Boehm, Surface oxides on carbon and their analysis: a critical assessment, *Carbon N. Y.* 40 (2002) 145–149, [https://doi.org/10.1016/S0008-6223\(01\)00165-8](https://doi.org/10.1016/S0008-6223(01)00165-8).
- Y. Zhang, H. Feng, X. Wu, L. Wang, A. Zhang, T. Xia, H. Dong, X. Li, L. Zhang, Progress of electrochemical capacitor electrode materials: a review, *Int. J. Hydrogen Energy* 34 (2009) 4889–4899, <https://doi.org/10.1016/j.ijhydene.2009.04.005>.
- J. Chmiola, G. Yushin, Y. Gogotsi, C. Portet, P. Simon, P.L. Taberna, Anomalous increase in carbon at pore sizes less than 1 nanometer, *Science* 313 (2006) 1760–1763, <https://doi.org/10.1126/science.1132195>.
- T. Aida, K. Yamada, M. Morita, An advanced hybrid electrochemical capacitor that uses a wide potential range at the positive electrode, *Electrochem. Solid St.* 9 (2006) 534–536, <https://doi.org/10.1149/1.2349495>.
- M.N. Collins, M. Nechifor, F. Tanasă, M. Zănoagă, A. McLoughlin, M.A. Stróżyk, M. Culebras, C.A. Teacă, Valorization of lignin in polymer and composite systems for advanced engineering applications – a review, *Int. J. Biol. Macromol.* 131 (2019) 828–849, <https://doi.org/10.1016/j.IJBIOMAC.2019.03.069>.
- B. Zhou, W. Liu, Y. Gong, L. Dong, Y. Deng, High-performance pseudocapacitors from kraft lignin modified active carbon, *Electrochim. Acta* 320 (2019) 134640, <https://doi.org/10.1016/j.electacta.2019.134640>.
- S. Sopčić, D. Antičić, Z. Mandić, Effects of the composition of active carbon electrodes on the impedance performance of the AC/AC supercapacitors, *J. Solid State Electrochem.* 26 (2022) 591–605, <https://doi.org/10.1007/s10008-021-05112-8>.
- H. Gu, Y.E. Zhu, J. Yang, J. Wei, Z. Zhou, Nanomaterials and technologies for lithium-ion hybrid supercapacitors, *ChemNanoMat* 2 (2016) 578–587, <https://doi.org/10.1002/cnma.201600068>.
- S. Koohi-Fayegh, M.A. Rosen, A review of energy storage types, applications and recent developments, *J. Energy Storage.* 27 (2020), <https://doi.org/10.1016/J.EST.2019.101047>.
- M. Karnan, A.G.K. Raj, K. Subramani, S. Santhoshkumar, M. Sathish, The fascinating supercapacitive performance of activated carbon electrodes with enhanced energy density in multifarious electrolytes, *Sustain. Energy Fuels* 4 (2020) 3029–3041, <https://doi.org/10.1039/c9se01298b>.
- L.A. Zevallos Torres, A. Lorenci Woiciechowski, V.O. de Andrade Tanobe, S. G. Karp, L.C. Guimarães Lorenci, C. Faulds, C.R. Soccol, Lignin as a potential source of high-added value compounds: a review, *J. Clean. Prod.* 263 (2020), <https://doi.org/10.1016/j.jclepro.2020.121499>.
- N. Izaguirre, E. Robles, R. Llano-Ponte, J. Labidi, X. Erdocia, Fine-tune of lignin properties by its fractionation with a sequential organic solvent extraction, *Ind. Crop. Prod.* 175 (2022) 114251, <https://doi.org/10.1016/j.indcrop.2021.114251>.
- T.S. Mathis, N. Kurra, X. Wang, D. Pinto, P. Simon, Y. Gogotsi, Energy storage data reporting in perspective—guidelines for interpreting the performance of electrochemical energy storage systems, *Adv. Energy Mater.* 9 (2019) 1–13, <https://doi.org/10.1002/aenm.201902007>.
- S. Xiao-mei, Z. Shu-quan, Z. Wen-hui, Effect of surface modification of activated carbon on its adsorption capacity for NH₃, *J. China Univ. Min. Technol.* 18 (2007) 261–274, <https://doi.org/10.1080/19443994.2012.749052>.
- P. Suktha, P. Chiochan, P. Pamprasertkun, J. Wutthiprom, N. Phattharasupakun, M. Suksomboon, T. Kaewsongpol, P. Sirisundomkit, T. Pettong, M. Sawangphruk, High-performance supercapacitor of functionalized carbon fiber paper with high surface ionic and bulk electronic conductivity: effect of organic functional groups, *Electrochim. Acta* 176 (2015) 504–513, <https://doi.org/10.1016/j.electacta.2015.07.044>.
- T.Z. Ren, L. Liu, Y. Zhang, Z.Y. Yuan, Nitric acid oxidation of ordered mesoporous carbons for use in electrochemical supercapacitors, *J. Solid State Electrochem.* 17 (2013) 2223–2233, <https://doi.org/10.1007/s10008-013-2088-1>.
- A. Lisovskii, G.E. Shter, R. Semiat, C. Aharoni, Adsorption of sulfur dioxide by active carbon treated by nitric acid: II. Effect of preheating on the adsorption

- properties, Carbon N. Y. 35 (1997) 1645–1648, [https://doi.org/10.1016/S0008-6223\(97\)00122-X](https://doi.org/10.1016/S0008-6223(97)00122-X).
- [35] P. Bober, N. Gavrilov, A. Kovalcik, M. Mičušík, C. Unterweger, I.A. Pašti, I. Seděnková, U. Acharya, J. Pflieger, S.K. Filippov, J. Kuliček, M. Omastová, S. Breitenbach, G. Čirić-Marjanović, J. Stejskal, Electrochemical properties of lignin/polypyrrole composites and their carbonized analogues, Mater. Chem. Phys. 213 (2018) 352–361, <https://doi.org/10.1016/j.materchemphys.2018.04.043>.
- [36] M. Mithun Kumar, L. Gurralla, C. Paek, R. Vinu, Selective production of guaiacol from lignin via catalytic transfer hydrogenolysis using Ru-Cu/Zirconia, Mol. Catal. 530 (2022) 112532, <https://doi.org/10.1016/j.mcat.2022.112532>.
- [37] F. Ciucci, Modeling electrochemical impedance spectroscopy, Curr. Opin. Electrochem. 13 (2019) 132–139, <https://doi.org/10.1016/j.coelec.2018.12.003>.
- [38] M. Saccoccio, T.H. Wan, C. Chen, F. Ciucci, Optimal regularization in distribution of relaxation times applied to electrochemical impedance spectroscopy: Ridge and Lasso regression methods - a theoretical and experimental study, Electrochim. Acta 147 (2014) 470–482, <https://doi.org/10.1016/j.electacta.2014.09.058>.
- [39] E. Ivers-Tiffée, A. Weber, Evaluation of electrochemical impedance spectra by the distribution of relaxation times, J. Ceram. Soc. Japan. 125 (2017) 193–201, <https://doi.org/10.2109/jcersj2.16267>.
- [40] D. Klotz, J.P. Schmidt, A. Weber, E. Ivers-Tiffée, The distribution of relaxation times as beneficial tool for equivalent circuit modelling of batteries and fuel cells, in: ECS Meet. Abstr. MA2011-02, 2011, p. 2611, <https://doi.org/10.1149/ma2011-02/46/2611>.
- [41] A. Weiß, S. Schindler, S. Galbiati, M.A. Danzer, R. Zeis, Distribution of relaxation times analysis of high-temperature PEM fuel cell impedance spectra, Electrochim. Acta 230 (2017) 391–398, <https://doi.org/10.1016/j.electacta.2017.02.011>.
- [42] S. Dierickx, A. Weber, E. Ivers-Tiffée, How the distribution of relaxation times enhances complex equivalent circuit models for fuel cells, Electrochim. Acta 355 (2020) 136764, <https://doi.org/10.1016/j.electacta.2020.136764>.
- [43] M.A. Danzer, Generalized distribution of relaxation times analysis for the characterization of impedance spectra, Batteries 5 (2019) 1–16, <https://doi.org/10.3390/batteries5030053>.
- [44] G. Ragoisha, Y. Aniskevich, Comment to the article “How to measure and report the capacity of electrochemical double layers, supercapacitors, and their electrode materials” [1], J. Solid State Electrochem. 25 (2021) 753, <https://doi.org/10.1007/s10008-020-04880-z>.
- [45] G.K. Mishra, R. Kant, Modular theory for DC-biased electrochemical impedance response of supercapacitor, J. Power Sources 473 (2020), <https://doi.org/10.1016/j.jpowsour.2020.228467>.
- [46] Y. Ge, X. Xie, J. Roscher, R. Holze, Q. Qu, How to measure and report the capacity of electrochemical double layers, supercapacitors, and their electrode materials, J. Solid State Electrochem. 24 (2020) 3215–3230, <https://doi.org/10.1007/s10008-020-04880-z>.
- [47] F. Yu, T. Huang, P. Zhang, Y. Tao, F.Z. Cui, Q. Xie, S. Yao, F. Wang, Design and synthesis of electrode materials with both battery-type and capacitive charge storage, Energy Storage Mater. 22 (2019) 235–255, <https://doi.org/10.1016/j.ensm.2019.07.023>.
- [48] A.J. Bard, L.R. Faulkner, H.S. White, *Electrochemical Methods: Fundamentals and Applications*, Wiley, 2022.
- [49] C. Largeot, C. Portet, J. Chmiola, P.L. Taberna, Y. Gogotsi, P. Simon, Relation between the ion size and pore size for an electric double-layer capacitor, J. Am. Chem. Soc. 130 (2008) 2730–2731, <https://doi.org/10.1021/ja7106178>.
- [50] H. Wang, J. Wen, Biomass porous carbon-based composite for high performance supercapacitor, Mater. Res. Express. 7 (2020), <https://doi.org/10.1088/2053-1591/abc442>.